Localised waves in elastic plates with perturbed honeycomb arrays of constraints

S. G. Haslinger[1], S. Frecentese[1] and G. Carta[2]

Abstract

In this paper, we study wave propagation in elastic plates incorporating honeycomb arrays of rigid pins. In particular, we demonstrate that topologically non-trivial band-gaps are obtained by perturbing the honeycomb arrays of pins such that the ratio between the lattice spacing and the distance of pins is less than 3; conversely, a larger ratio would lead to the appearance of trivial stop-bands. For this purpose, we investigate band inversion of modes and calculate the valley Chern numbers associated with the dispersion surfaces near the band opening, since the present problem has analogies with the quantum valley Hall effect. In addition, we determine localised eigenmodes in strips, repeating periodically in one direction, that are subdivided into a topological and a trivial section. Finally, the outcomes of the dispersion analysis are corroborated by numerical simulations, where a time-harmonic point source is applied to a plate with finite arrays of rigid pins to create localised waves immune to backscattering.

1 Introduction

Topologically protected wave propagation in elastic metamaterials has attracted increasing attention in the scientific community in recent years, due to the possibility of creating waveguides that are immune to backscattering in the presence of defects, such as impurities or sharp corners. The idea was firstly proposed in quantum mechanics [1, 2] and later extended to photonic [2, 3, 4, 5, 6] and acoustic [7, 8, 9, 10, 11, 12] media.

In elasticity, different classes of passive models have been proposed to realise topologically protected edge states, such as lattices [13, 14, 15] and plates [16, 17]. In the latter type of structures, topological supernetworks with tunable directionality, based on combinations of multi-directional energy splitters, have been designed in [18, 19, 20] using group theory, topological concepts and tunnelling phenomena. Edge waves have been observed in discrete lattices including tilted resonators in [21, 22], while wave localisation in lattices of Rayleigh beams has been investigated in [23, 24, 25]. Localised folding motions at the boundaries of origami and kirigami structures have been connected to topological polarisation in [26]. Topological properties of rotational waves in granular crystals have been discussed in [27]. Valley anisotropy has been observed in [28], where a chiral system consisting of hard spiral scatterers embedded in a soft material matrix has been studied.

The systems mentioned above, comprising only passive elements, do not break time-reversal symmetry. The latter can be broken if active components are also incorporated or if an external field with a momentum bias is applied to the system. For instance, in [29] a lattice model has been employed to describe topologically protected edge modes in microtubules, present in eukaryotic cells, where time-reversal symmetry can be broken by weak magnetic properties of the tubulin proteins. Gyroscopic action can also be used in this framework to create topological

insulators, as demonstrated in [30, 31, 32, 33, 34, 35, 36, 37] for elastic lattices and in [38, 39] for elastic plates.

In this paper, we consider an elastic plate constrained by a periodic arrangement of honeycomb arrays of rigid pins. Dirac cones are broken by perturbing the positions of the pins, and as a consequence a stop-band is generated. Following the concept proposed in [40] and developed for a honeycomb array of dielectric cylinders in a material with different dielectric properties, we alter the locations of the pins to create either a topological or a trivial band-gap in proximity of the broken Dirac cone.

The topology of Dirac cones in pinned elastic plates has been extensively investigated in [41, 42], where unidirectional trapped modes have also been observed. Wave transmission in elastic plates incorporating periodic arrays of rigid pins or masses have been studied in [43, 44, 45], while localisation phenomena produced by semi-infinite grating stacks of pins or different types of oscillators have been examined in [46, 47, 48]. The possibility of attaching active sources to a plate with the purpose of designing an optimal cloaking device has been proposed in [49]. The effect of cavities on the band diagram of a platonic crystal has been analysed in [50, 51], both numerically and experimentally, while the band structures of thin and thick plates connected to periodic systems of spring-mass resonators have been obtained in [52, 53]. Homogenised models to describe flexural vibrations localised in single or double rings of spring-mass resonators have been formulated in [54] and [55], respectively, based on pointwise descriptions of dynamic fields of the meso-scale type [56, 57].

The paper is organised as follows. After presenting the model in Section 2, we discuss the dispersion properties for both the unperturbed and perturbed systems in Section 3, focussing the attention on the band inversion of modes. Then, in Section 4 we calculate the valley Chern numbers to distinguish between topological and trivial regimes. In Section 5 we show localised interfacial modes in periodic strips divided into a topological and a trivial region, and in Section 6 we illustrate topologically robust waves that are immune to backscattering. Finally, in Section 7 we provide concluding remarks.

2 Motivation for the work and description of the model

We consider the Kirchhoff-Love elastic plate analogue of a topological photonic crystal, made purely of conventional dielectric material, which was proposed in [40]. In particular, in [40] a honeycomb array of cylinders with dielectric constant ε_d is embedded within a surrounding medium characterised by different dielectric constant ε_a. The unperturbed honeycomb lattice (generated by a primitive rhombic unit cell) is illustrated in Fig. 1(a), where neighbouring cylinders are separated by R. Introducing the lattice constant a_0, the system is equivalent to a triangular lattice of hexagonal cells composed of six neighbouring cylinders when $a_0/R = 3$. Taking this larger hexagonal macrocell as the unit cell, the Dirac cones arising at the K and K' points in the first Brillouin zone of the honeycomb lattice, shown in Fig. 1(b), are folded into doubly degenerate Dirac cones at the Γ point ($k_x = k_y = 0$) for the macrocell treatment [41, 58]. By varying the lattice parameter a_0/R, the triangular lattice of hexagonal cells is deformed in such a way as to preserve both the triangular lattice and the C_6 symmetry, but leads to anisotropy, including the opening of a non-trivial band-gap at the quadruply degenerate Dirac point.

Here, we study the same periodic structure but replace the dielectric photonic crystal with a platonic crystal, where a thin elastic plate is structured with an array of rigid pins (zero displacement at point scatterers). Using the biharmonic model for flexural wave propagation in

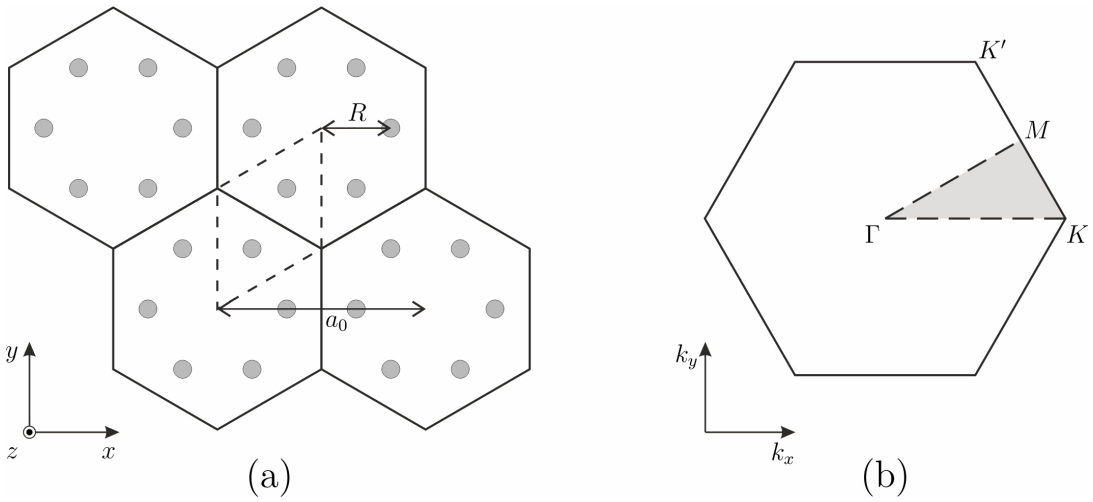

Figure 1: (a) Unperturbed honeycomb array, that can be generated by either a rhombic (dashed) or hexagonal macrocell. In the latter case, it is characterised by the lattice parameter $a_0/R = 3$, where a_0 is the spacing between the centres of neighbouring hexagonal macrocells, and R is the distance of an individual cylinder from its cell's centre. (b) First Brillouin zone for the triangular lattice in the reciprocal space. Dirac cones arise at the K and K' points.

Kirchhoff-Love plates, the governing equation for the out-of-plane displacement $u(\boldsymbol{r})$ is expressed by

$$\Delta^2 u(\boldsymbol{r}) - \frac{\rho h \omega^2}{D} u(\boldsymbol{r}) = 0, \tag{1}$$

where Δ represents the Laplacian operator, ρ is the density (mass per unit volume), h is the thickness and $D = Eh^3/(12(1-\nu^2))$ is the flexural rigidity of the plate, with E and ν being the Young's modulus and Poisson's ratio, respectively. In addition, $\boldsymbol{r}$ is the position vector and ω is the angular frequency. The spectral parameter β is often employed, and its relations with both ω and the frequency f are given by

$$\beta^2 = \omega \sqrt{\frac{\rho h}{D}}, \quad f = \frac{\omega}{2\pi}. \tag{2}$$

We point out that the spectral parameter β has the dimensions of a wavenumber.

Regarding the honeycomb array of point constraints, by increasing a_0/R we squeeze the rigid pins closer together (see Fig. 2(a) for $a_0/R = 3.5$), producing a triangular lattice of regular hexagonal cells. Reducing the lattice parameter has the opposite effect, stretching the triangular lattice's constituent hexagonal cells (see Fig. 2(b) for the case $a_0/R = 2.5$). Note that the perturbation of Fig. 1(a)'s pure honeycomb structure results in irregular hexagons between the triangular lattice's regular hexagonal macrocells, whose size and nature depend on the choice of whether to reduce or increase a_0/R. The limiting cases are shown in Figs. 2(c,d): in part (c), we illustrate the case $a_0/R = 10$, which demonstrates that in the limit as $a_0/R \to \infty$, the lattice approaches the pure hexagonal Bravais lattice; the same result occurs for the limiting case $a_0/R \to 1$, shown in part (d).

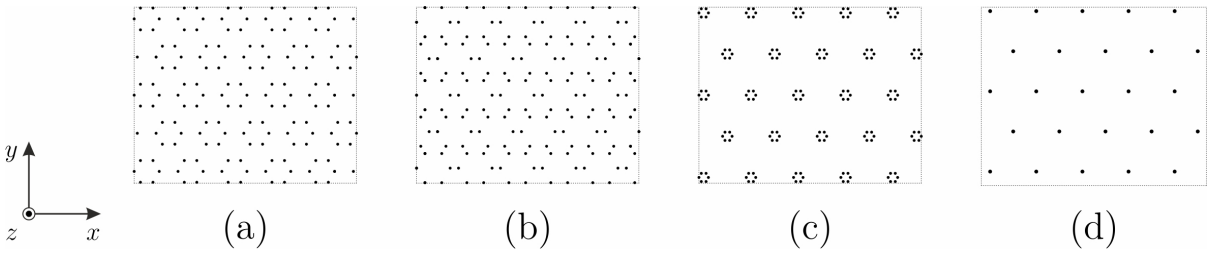

Figure 2: Comparison of perturbed honeycomb lattices: (a) $a_0/R = 3.5$, (b) $a_0/R = 2.5$, (c) $a_0/R = 10$, (d) $a_0/R = 1$.

3 Dispersion properties

The dispersion diagrams and eigenmodes of the unperturbed and perturbed structured plates are determined numerically using the finite element package *Comsol Multiphysics*. To this aim, Bloch-Floquet conditions are applied at the boundaries of the periodic cell [38, 39, 46]. In the following, we consider an aluminum plate having Young's modulus $E = 70$ GPa, Poisson's ratio $\nu = 0.33$, density $\rho = 2700$ kg/m^3 and thickness $h = 0.002$ m. The lattice constant is taken as $a_0 = 1$ m.

3.1 Unperturbed array of rigid pins

The dispersion diagram for the unperturbed honeycomb system with the hexagonal macrocell defined by $a_0/R = 3$, computed along the path $\Gamma K M \Gamma$ (see Fig. 1(b)), is shown in Fig. 3(a). The corresponding dispersion surfaces near Γ are illustrated in Fig. 3(b), where we plot the spectral parameter β on the vertical axis versus the wavevector components k_x and k_y on the horizontal axes. Note that the presence of the rigid pins leads to a low-frequency band-gap for $\beta < 7.25$ m^{-1}. We also observe another significant band-gap for this system for 9.34 m^{-1} $\leq \beta \leq 10.88$ m^{-1}. The most striking feature of Figs. 3(a) and 3(b) is the quadruply degenerate Dirac point at $\Gamma = (k_x, k_y) = (0, 0)$ for $\beta \simeq 12.56$ m^{-1}, where two doubly degenerate Dirac cones meet (the dispersion diagram in part (a) is illustrated in the interval $\beta \in [11, 15]$ (m^{-1}) to better illustrate the Dirac point). This is analogous to the double Dirac cones identified in [40] for the photonic honeycomb crystal, and is also reminiscent of the multiply degenerate Dirac points observed in [41] for elastic plates pinned at points of a hexagonal lattice (although in [41] an additional flat band surface, passing through the Dirac-like point, is also present).

In Fig. 3(c), we illustrate the system's Bloch modes in proximity of the Dirac point frequency at the Γ-point. The two modes for $\beta = 12.557$ m^{-1} (or, equivalently, $f = 78.156$ Hz), which are associated with the apex of the lower cone in Fig. 3(b), are denoted by $\lambda^\dagger$ and $\lambda^\ddagger$. In contrast, the two modes for $\beta = 12.558$ m^{-1} (corresponding to $f = 78.159$ Hz), which belong to the upper cone in Fig. 3(b), are indicated by $\lambda^\odot$ and λ^*.

3.2 Perturbed arrays of rigid pins

For the analogous photonic crystal discussed in [40], reducing the lattice parameter (namely, taking $a_0/R < 3$) opens a global band-gap near the Dirac point, and a band inversion takes place - this is referred to as the *topological* regime in [40]. Conversely, for the opposite type of perturbation (such that $a_0/R > 3$), no band inversion takes place, and this is called the *trivial* regime. These contrasting scenarios are determined by the $p_\pm$ and $d_\pm$ states for the electromagnetic

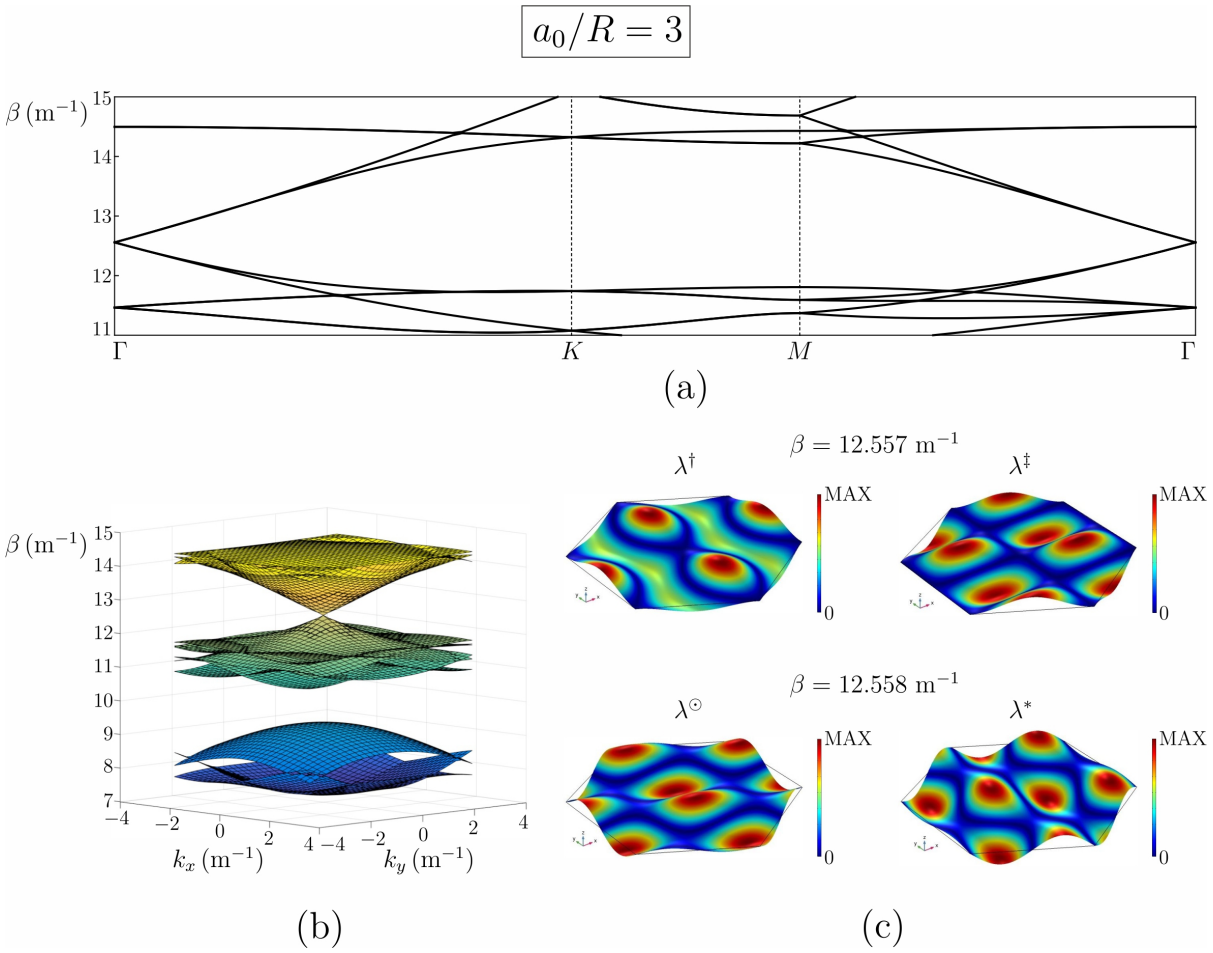

Figure 3: (a) Dispersion diagram for the unperturbed honeycomb lattice (generated equivalently by rhombic or hexagonal macrocell) with $a_0/R = 3$, evaluated along the path $\Gamma KM\Gamma$ and shown in the range $\beta \in [11, 15]$ (m^{-1}). (b) Dispersion surfaces for the same structure, shown in the range $\beta \in [7, 15]$ (m^{-1}). (c) Eigenmodes associated with the Dirac point at $\beta \simeq 12.56$ m^{-1}. For $\beta = 12.557$ m^{-1} (slightly below the Dirac point), the two modes are denoted by $\lambda^{\dagger}$ and $\lambda^{\ddagger}$; for $\beta = 12.558$ m^{-1} (slightly above the Dirac point), we use $\lambda^{\odot}$ and λ^{*}.

dielectric case. Specifically, solving the Maxwell equations yields harmonic transverse magnetic (TM) modes that are supported by the hexagonal cells, which act as "artificial atoms" in the present geometry. The modes exhibit orbital-like p- and d-wave shapes, hence the terminology adopted in [40] to distinguish between the types of mode, and form photonic bands.

For the platonic case here, perturbing the array of pins leads to the opening of a band-gap around the Dirac point at $\Gamma = (0, 0)$. When $a_0/R = 2.85$ (see Figs. 4(a) and 4(b)), the stop-band is in the range $\beta \in [12.58, 12.74]$ (m^{-1}). On the other hand, when $a_0/R = 3.25$ (see Figs. 4(d) and 4(e)), the band-gap is narrower: $\beta \in [12.68, 12.78]$ (m^{-1}).

The eigenmodes demonstrate something analogous to the photonic crystal's band inversion. For $a_0/R = 3.25$, equivalent to the *trivial* regime in [40], the modes below ($\lambda^{\dagger}$ and $\lambda^{\ddagger}$) and above ($\lambda^{\odot}$ and λ^{*}) the band opening at $\Gamma = (0, 0)$ are similar to those found for the unperturbed array of pins (compare Figs. 3(c) and 4(f)). Conversely, for the *topological* regime ($a_0/R = 2.85$), the modes $\lambda^{\odot}$ and λ^{*} arise at a lower frequency than $\lambda^{\dagger}$ and $\lambda^{\ddagger}$, as shown in Fig. 4(c). A band inversion takes place around the Dirac point, and so a non-trivial band-gap is obtained, by perturbing the periodicity with $a_0/R < 3$.

4 Calculation of valley Chern number

In order to compute the valley Chern number, we follow a procedure similar to that developed in [30, 28]. The considered elastic periodic plate, constrained by arrays of rigid pins, is a continuous structure, that is discretised with the finite element method to determine numerically the dispersion diagrams. For each dispersion surface, we can obtain the eigenvector $\boldsymbol{W} = \boldsymbol{W}(\boldsymbol{k})$ corresponding to any value of the wavevector $\boldsymbol{k} = (k_x, k_y)^{\mathrm{T}}$ and to the specific value of the frequency $\omega = \omega(\boldsymbol{k})$ associated with that dispersion surface.

Since the system has time-reversal symmetry, the integration of the Berry curvature $\Omega(\boldsymbol{k})$ (defined below) over the Brillouin zone is zero; however, $\Omega(\boldsymbol{k})$ is localised near the valleys (in particular, at the K and K' points), hence the integration over a small area around the valley results in a non-zero value [28]. This integration is denoted as the *valley Chern number* [28]:

$$C_v = \frac{1}{2\pi} \int_{\mathcal{S}} \Omega(\boldsymbol{k}) \mathrm{d}^2\boldsymbol{k}, \tag{3}$$

where $\mathcal{S}$ is a small area around the valley.

The valley Chern number is calculated as follows. First, we consider the regions pertinent to the K and K' points in the reciprocal space, corresponding to the triangles indicated by T_1 and T_2 in Fig. 5. More specifically, the triangle T_1 has its vertices at the points $(k_x, k_y) = (0, 0)$, $\big(2\pi/a_0, -2\pi/(\sqrt{3}a_0)\big)$ and $\big(2\pi/a_0, 2\pi/(\sqrt{3}a_0)\big)$, while for the triangle T_2 the vertices are at the points $(k_x, k_y) = (0, 0)$, $\big(2\pi/a_0, 2\pi/(\sqrt{3}a_0)\big)$ and $\big(0, 4\pi/(\sqrt{3}a_0)\big)$. Then, we discretise each triangle into triangular and square facets, whose base and height are sufficiently small (in our calculations, they are equal to $[2\pi/a_0]/12$ and $[2\pi/(\sqrt{3}a_0)]/12$, respectively). For each square facet (for the triangular ones similar considerations apply, taking into account three points instead of four), we determine the eigenvectors at the $\boldsymbol{k}$-points corresponding to the vertices of the square facet, indicated by P_1, P_2, P_3 and P_4, taken along a counter-clockwise path. The Berry curvature is evaluated as [30]

$$\Omega(\boldsymbol{k}) = -\mathrm{Im}\left(\log\left[\frac{\langle \boldsymbol{W}(P_1)|\boldsymbol{W}(P_2)\rangle\langle \boldsymbol{W}(P_2)|\boldsymbol{W}(P_3)\rangle\langle \boldsymbol{W}(P_3)|\boldsymbol{W}(P_4)\rangle\langle \boldsymbol{W}(P_4)|\boldsymbol{W}(P_1)\rangle}{\langle \boldsymbol{W}(P_1)|\boldsymbol{W}(P_1)\rangle\langle \boldsymbol{W}(P_2)|\boldsymbol{W}(P_2)\rangle\langle \boldsymbol{W}(P_3)|\boldsymbol{W}(P_3)\rangle\langle \boldsymbol{W}(P_4)|\boldsymbol{W}(P_4)\rangle}\right]\right). \tag{4}$$

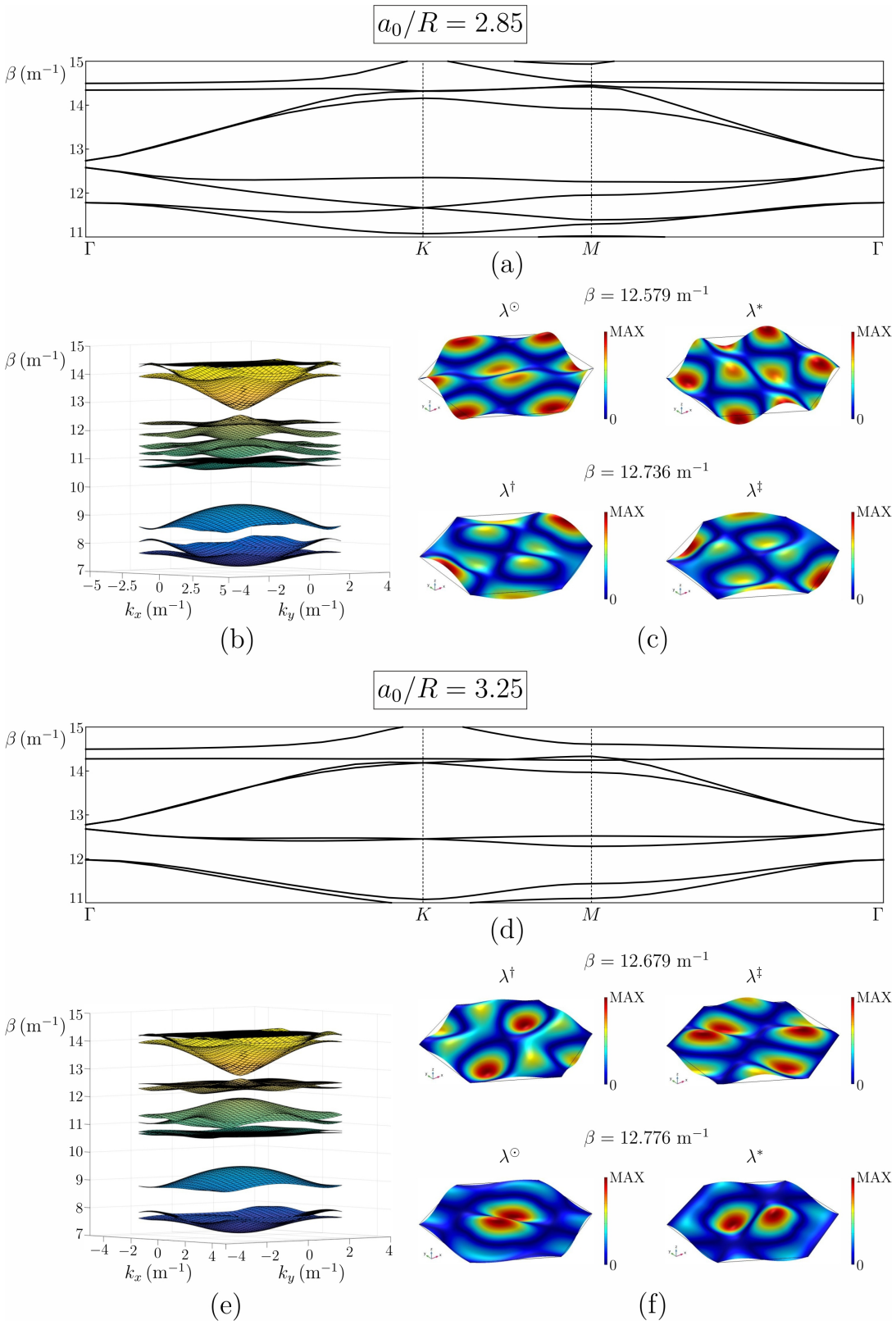

Figure 4: Results for perturbed honeycomb lattices, produced by varying the lattice parameter: (a-c) $a_0/R = 2.85$, (d-f) $a_0/R = 3.25$. (a,d) Dispersion diagrams. (b,e) Dispersion surfaces. (c,f) Eigenmodes in the vicinity of the band opening around the Dirac point at $\Gamma = (0, 0)$; the modes similar to those of the unperturbed honeycomb array in Fig. 3(c) are labelled in the same way with $\lambda^{\dagger}$, $\lambda^{\ddagger}$, $\lambda^{\odot}$ and λ^{*}.

Table 1: Valley Chern number C_v, computed for $a_0/R = 2.85$.

area	point	disp. surf. 8	disp. surf. 9	$\mathbf{8+9}$	disp. surf. 10	disp. surf. 11	$\mathbf{10+11}$
T_1	Γ	0.5	-0.5	**0**	-0.5	0.5	**0**
	K	-0.5	0	$\mathbf{-0.5}$	0	0.5	**0.5**
T_2	Γ	0.5	-0.5	**0**	0	0	**0**
	K'	0.5	0	**0.5**	0	-0.5	$\mathbf{-0.5}$

In the formula above,

$$\langle \boldsymbol{W}(P_i)|\boldsymbol{W}(P_j)\rangle = \int_A \boldsymbol{W}^*(\boldsymbol{k}|_{P_i}) \cdot \boldsymbol{W}(\boldsymbol{k}|_{P_j}) \mathrm{d}A, \tag{5}$$

where * denotes the complex conjugate and A is the area of the periodic cell. Note that the Berry curvature in (4) is intended to be associated with the eigenvector $\boldsymbol{k}$ at the middle point of the square facet. For the triangular facets, the Berry curvature is similarly evaluated at their centre.

In Fig. 5 we show the colour maps of the Berry curvature over the regions T_1 and T_2, relative to the honeycomb arrays with lattice parameters $a_0/R = 2.85$ (parts (a)-(d)) and $a_0/R = 3.25$ (parts (e)-(h)). In particular, four dispersion surfaces from Fig. 4(b,e) have been considered: the 8^{th} (Fig. 5 parts (a) and (e)), the 9^{th} (parts (b) and (f)), the 10^{th} (parts (c) and (g)) and the 11^{th} (parts (d) and (h)). For both values of the lattice parameter, the eighth and ninth dispersion surfaces lie below the band-gap generated by the perturbation imposed on the pins' locations, and they converge to each other at point Γ. Conversely, the tenth and eleventh dispersion surfaces are above the same band-gap and share a common point at Γ. Looking at Fig. 5, we observe clear localisations of $\Omega(\boldsymbol{k})$ at particular positions of the reciprocal space, in particular at Γ, K and K'.

The values of the valley Chern number C_v for the lattice parameter $a_0/R = 2.85$ are given in Table 1. We have also reported the sums of C_v of the 8^{th} and 9^{th} dispersion surfaces, below the band-gap, and of the 10^{th} and 11^{th} dispersion surfaces, above the band-gap. We note that the combined valley Chern numbers at Γ, in both T_1 and T_2, are zero. Conversely, at K the combined C_v for the two dispersion surfaces below the band-gap is -0.5, while for the two dispersion surfaces above the band-gap, it is equal to 0.5. The valley Chern numbers at K' are flipped in sign with respect to those at K, so that the Chern number over the whole Brillouin zone is zero, as expected. The non-trivial values of Chern numbers predict the presence of topologically protected valley edge modes, as also demonstrated in the following sections. This is in accordance with what has been observed in other elastic systems (see, for instance, [15, 16, 28]).

Concerning the results for the lattice parameter $a_0/R = 3.25$, given in Table 2, we note that the combined valley Chern numbers are zero at all points. This confirms that for $a_0/R > 3$ edge modes are not topologically protected (*trivial* regime).

5 Localised modes in infinite systems

Now, we investigate the dispersive properties of a system containing two sub-domains with different perturbations of the pins' locations: $a_0/R = 2.85$ (topological region) and $a_0/R = 3.25$ (trivial region). The number of rows of topological hexagonal cells is 19, while the trivial section contains 14 rows. We assume that the plate is infinite in the x-direction (see Fig. 6(a)), hence

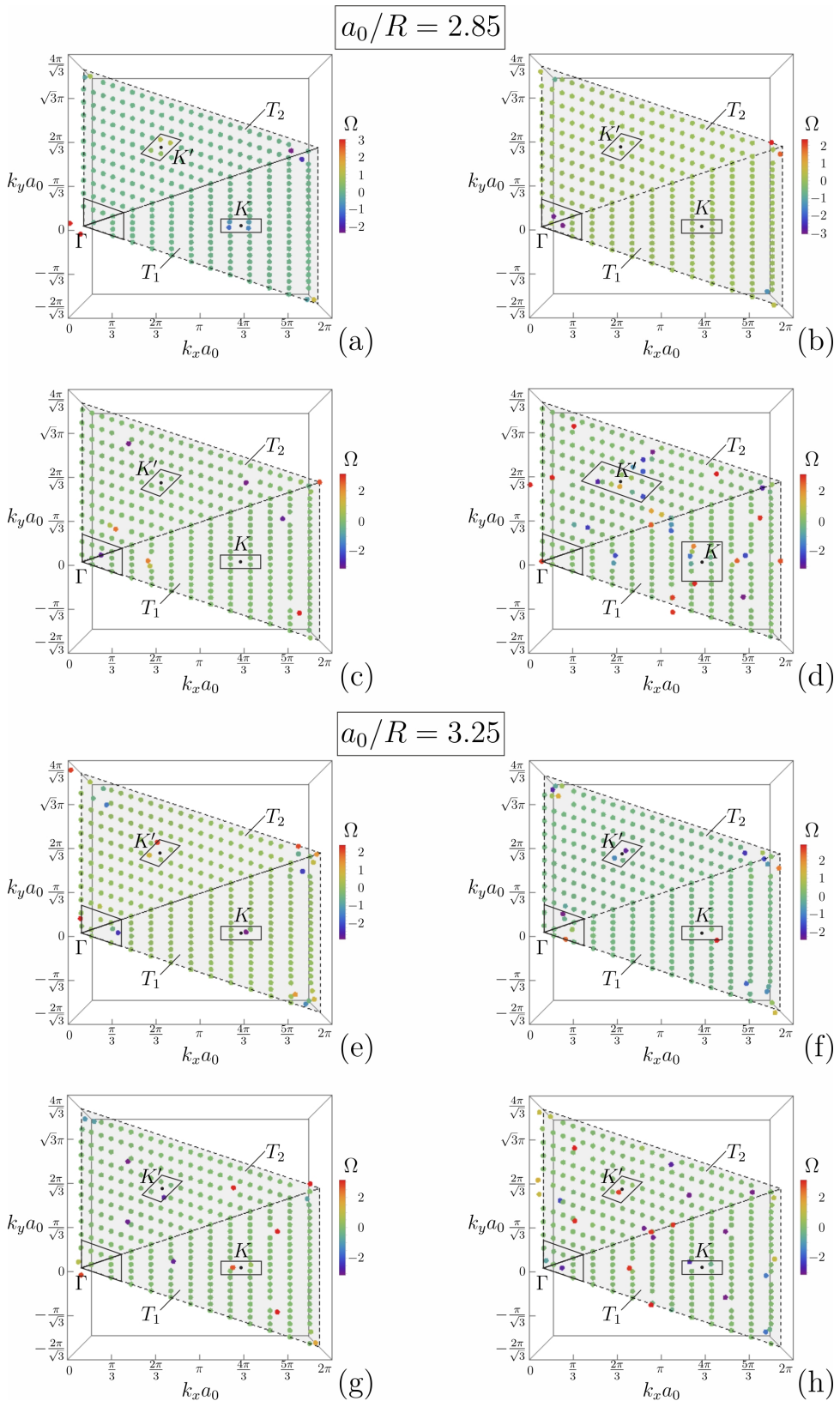

Figure 5: Maps of the Berry curvature $\Omega(\boldsymbol{k})$ for the lattice parameters (a-d) $a_0/R = 2.85$ and (e-h) $a_0/R = 3.25$, corresponding to the (a,e) 8^{th}, (b,f) 9^{th}, (c,g) 10^{th} and (d,h) 11^{th} dispersion surface. The triangles T_1 and T_2 are the areas of pertinence of the K and K' points, respectively. The areas around the points Γ, K and K', delimited by solid thick lines, indicate the regions where the valley Chern numbers have been calculated.

Table 2: Valley Chern number C_v, computed for $a_0/R = 3.25$.

area	point	disp. surf. 8	disp. surf. 9	**8 + 9**	disp. surf. 10	disp. surf. 11	**10 + 11**
T_1	Γ	-0.5	0.5	**0**	0.5	-0.5	**0**
	K	-0.5	0.5	**0**	0.5	-0.5	**0**
T_2	Γ	0.5	-0.5	**0**	0.2	-0.2	**0**
	K'	0.5	-0.5	**0**	-0.5	0.5	**0**

quasi-periodicity Bloch-Floquet conditions can be imposed at the boundaries of the parallelogram macrocell, shown by dashed lines. A homogeneous plate (namely, a plate without rigid pins) and a slab incorporating viscous dampers are inserted in proximity of each edge of the system.

Referring to the results reported in Section 33.2, we note that for this choice of the lattice parameters the topological and trivial regions share a common stop-band for $\beta \in [12.68, 12.74]$ (m^{-1}). This ensures that localised modes at the interface between the two regions (indicated by a dotted line in Fig. 6(a)) can be supported.

By performing an eigenfrequency analysis with *Comsol Multiphysics*, which provides the eigenfrequencies for varying wavenumber, we obtain the dispersion curves plotted in Fig. 6(b), where we show β versus k_x in the vicinity of the unperturbed honeycomb structure's Dirac point at Γ and $\beta = 12.56$ m^{-1}. We observe that additional modes appear in the mutual band-gap of the topological and trivial regions, and these are located at the interface where the topological and trivial parts meet. An example of an interfacial mode that decays exponentially into the bulk of the system is illustrated in Fig. 6(c).

6 Interfacial waves in finite clusters

In this section, we demonstrate the ability of these perturbed systems to transport energy with little leakage by modelling plates with finite clusters of pins that act as waveguides. By considering sufficiently large clusters, we can replicate the key properties of the infinite system illustrated in Fig. 6(a), and therefore show examples of localised interfacial modes.

We consider the finite system in Fig. 7(a), comprising 43×43 hexagonal cells of rigid pins, divided into a topological ($a_0/R = 2.85$) and a trivial ($a_0/R = 3.25$) region. The topological section consists of 24×24 hexagonal cells and is positioned in the top left corner. We apply a point source on the lateral interface (shown by a double arrow in Fig. 7(a)), characterised by a frequency $f = 79.814$ Hz (corresponding to $\beta = 12.69$ m^{-1}), which is inside the mutual stop-band of the topological and trivial regions. By plotting the displacement field in Fig. 7(a), we observe a wave that is localised at the interface, with little leakage into the surrounding medium. The robustness of the system is evidenced by the fact that wave propagation is not affected by the presence of geometrical defects, represented in this case by a corner in the interface.

In Fig. 7(b), we show the displacement field when the frequency parameter of the point source is $\beta = 12.63$ m^{-1}, which is in the stop-band for the topological array, but in the pass-band for the trivial one. We observe transmission into the latter section of the system, which highlights that the operating range for the interfacial modes is restricted to the overlapping band-gap for the constituent parts of the system.

In the Supplementary Material accompanying this paper, we show additional examples of interfacial waves, obtained for a couple of different values of the lattice parameters characterising the topological and trivial regions of the array of pins.

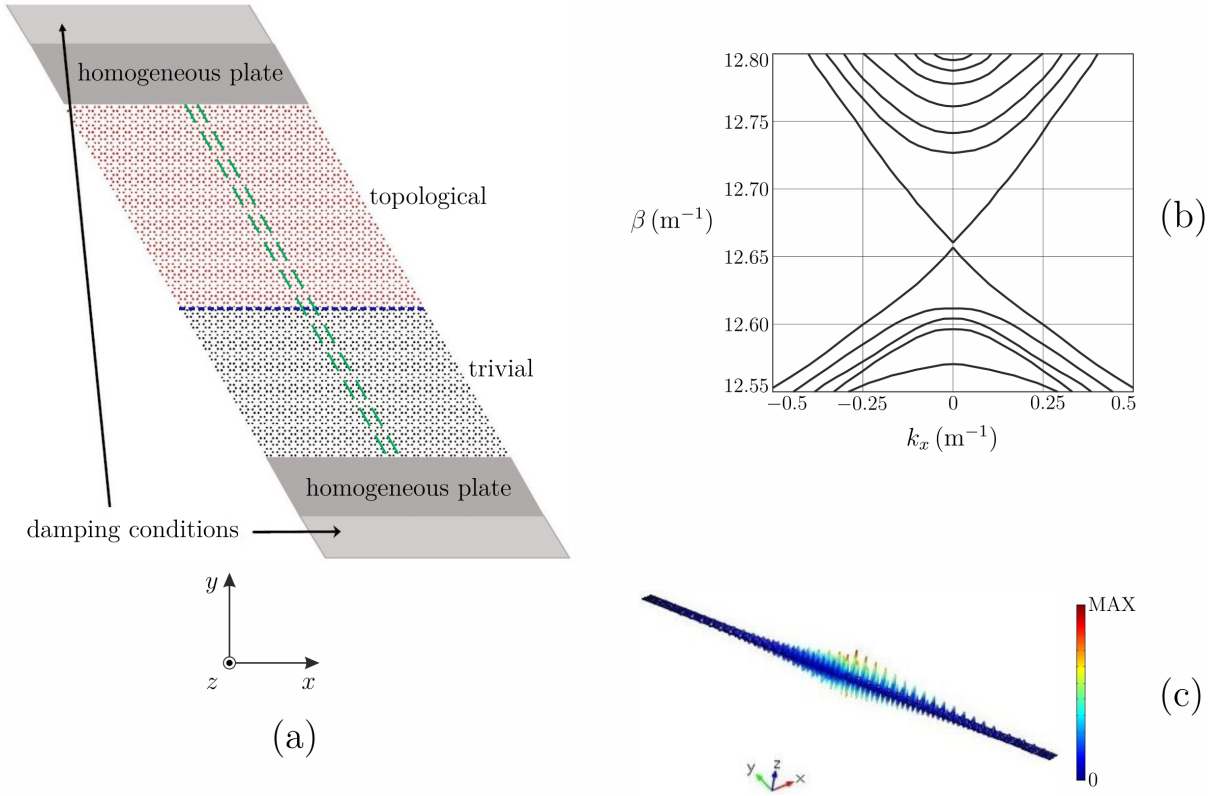

Figure 6: (a) Schematic diagram for an infinite plate in the x-direction, comprising a topological ($a_0/R = 2.85$) and a trivial ($a_0/R = 3.25$) region of perturbed honeycomb arrays of pins. Damping conditions are introduced near the top and bottom boundaries. The parallelogram macrocell is indicated by dashed lines. (b) Dispersion curves for the system in (a). (c) Example of an eigenmode localised at the interface between the topological and trivial regions, obtained for $\beta = 12.69$ m^{-1}.

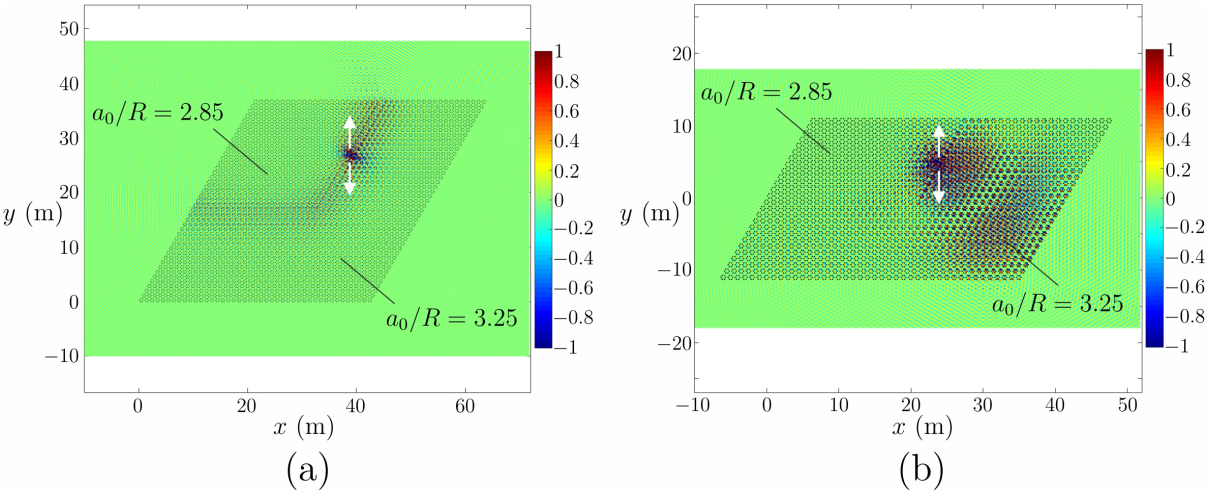

Figure 7: (a) Interfacial wave in an elastic plate with a 43×43 cluster of hexagonal cells of rigid pins, with the topological section consisting of 24×24 rows in the top left corner. The wave is generated by a harmonic force (shown by a double arrow) with a frequency parameter $\beta = 12.69$ m^{-1}. The lattice parameters are $a_0/R = 2.85$ in the topological region and $a_0/R = 3.25$ in the trivial region. (b) For $\beta = 12.63$ m^{-1}, there is no localised wave at the interface, the energy leaks into the trivial part. In this case, the plate incorporates a 42×26 cluster of pins, with the topological section being made of 21×13 rows in the top left corner.

7 Conclusions

We have shown how to perturb honeycomb arrays of pins in elastic plates to obtain either a topological or a trivial band-gap, in analogy with what has been observed in dielectric media containing hexagonal arrangements of cylinders with a different dielectric constant.

First, the study of band inversion and Berry curvatures, localised at specific points in the reciprocal space, has demonstrated that when the ratio of the lattice spacing to the distance between pins in the honeycomb topology is smaller (larger) than 3, a topological (trivial) band-gap opens up in the neighbourhood of the Dirac point of the unperturbed system's dispersion diagram. In addition, by analysing the dispersion properties of a strip of finite height and periodic in the perpendicular direction, that is also subdivided into a topological and a trivial section, we have observed modes localised at the interface between the two sections for frequencies falling inside the common band-gap of the topological and trivial sections. Finally, we have derived the response of an elastic plate with a large but finite array of pins, again arranged in two sub-regions with topological and trivial band-gaps, to a time-harmonic excitation imposed at the interface between the two regions, and we have observed a localised interfacial wave if the frequency of the excitation lies within the common band-gap. Hence, the proposed model is capable of supporting topologically protected edge and interfacial modes that are immune to backscattering.

We envisage that the results of the present work may have important implications in engineering applications related to wave guiding, vibration isolation and energy harvesting.

References

[1] Haldane FDM. 1988. Model for a quantum Hall effect without Landau levels: Condensed-matter realization of the parity anomaly. *Phys. Rev. Lett.* **61**, 2015.

[2] Raghu S, Haldane FDM. 2008. Analogs of quantum-Hall-effect edge states in photonic crystals. *Phys. Rev. A* **78**, 033834.

[3] Wang Z, Chong YD, Joannopoulos JD, Soljačić M. 2008. Reflection-free one-way edge modes in a gyromagnetic photonic crystal. *Phys. Rev. Lett.* **100**, 013905.

[4] He C, Chen XL, Lu MH, Li XF, Wan WW, Qian XS, Yin RC, Chen YF. 2010. Left-handed and right-handed one-way edge modes in a gyromagnetic photonic crystal. *J. Appl. Phys.* **107**, 123117.

[5] Khanikaev AB, Mousavi SH, Tse WK, Kargarian M, MacDonald AH, Shvets G. 2013. Photonic topological insulators. *Nature Mater.* **12**, 233–239.

[6] Gao W, Lawrence M, Yang B, Liu F, Fang F, Béri J, Li J, Zhang S. 2015. Topological photonic phase in chiral hyperbolic metamaterials. *Phys. Rev. Lett.* **114**, 037402.

[7] Khanikaev AB, Fluery R, Mousavi SH, Alú A. 2015. Topologically robust sound propagation in an angular-momentum-biased graphene like resonator lattice. *Nat. Commun.* **6**, 8260.

[8] Ni X, He C, Sun XC, Liu XP, Lu MH, Feng L, Chen YF. 2015. Topologically protected one-way edge mode in networks of acoustic resonators with circulating air flow. *New J. Phys.* **17**, 053016.

[9] Yang Z, Gao F, Shi X, Lin X, Gao Z, Chong Y, Zhang B. 2015. Topological acoustics. *Phys. Rev. Lett.* **114**, 114301.

[10] Chen ZG, Wu Y. 2016. Tunable topological phononic crystals. *Phys. Rev. Appl.* **5**, 054021.

[11] He C, Ni X, Ge H, Sun XC, Chen YB, Lu MH, Liu XP, Chen YF. 2016. Acoustic topological insulator and robust one-way sound transport. *Nature Phys.* **12**, 1124–1129.

[12] Souslov A, van Zuiden BC, Bartolo D, Vitelli V. 2017. Topological sound in active-liquid metamaterials. *Nature Phys.* **13**, 1091–1094.

[13] Süsstrunk R, Huber SD. 2015. Observation of phononic helical edge states in a mechanical topological insulator. *Science* **349**(6243), 47-50.

[14] Pal RK, Schaeffer M, Ruzzene M. 2016. Helical edge states and topological phase transitions in phononic systems using bi-layered lattices. *J. Appl. Phys.* **119**, 084305.

[15] Vila J, Pal RK, Ruzzene M. 2017. Observation of topological valley modes in an elastic hexagonal lattice. *Phys. Rev. B* **96**, 134307.

[16] Pal RK, Ruzzene M. 2017. Edge waves in plates with resonators: an elastic analogue of the quantum valley Hall effect. *New J. Phys.* **19**, 025001.

[17] Miniaci M, Pal RK, Manna R, Ruzzene M. 2019. Valley-based splitting of topologically protected helical waves in elastic plates. *Phys. Rev. B* **100**, 024304.

[18] Makwana MP, Craster RV. 2018. Geometrically navigating topological platonic modes around gentle and sharp bends. *Phys. Rev. B* **98**, 184105.

[19] Makwana MP, Craster RV. 2018. Designing multi-directional energy-splitters and topological valley supernetworks. *Phys. Rev. B* **98**, 235125.

[20] Tang K, Makwana MP, Craster RV, Sebbah P. 2020. Observations of symmetry-induced topological mode steering in a reconfigurable elastic plate. *Phys. Rev. B* **102**, 214103.

[21] Tallarico D, Trevisan A, Movchan NV, Movchan AB. 2017. Edge waves and localization in lattices containing tilted resonators. *Front. Mater.* **4**, 16.

[22] Tallarico D, Movchan NV, Movchan AB, Colquitt DJ. 2017. Tilted resonators in a triangular elastic lattice: chirality, Bloch waves and negative refraction. *J. Mech. Phys. Solids* **103**, 236–256.

[23] Piccolroaz A, Movchan AB, Cabras L. 2017. Rotational inertia interface in a dynamic lattice of flexural beams. *Int. J. Solids Struct.* **112**, 45–53.

[24] Bordiga G, Cabras L, Bigoni D, Piccolroaz A. 2019. Free and forced wave propagation in a Rayleigh-beam grid: Flat bands, Dirac cones, and vibration localization vs isotropization. *Int. J. Solids Struct.* **161**, 64–81.

[25] Bordiga G, Cabras L, Piccolroaz A, Bigoni D. 2021. Dynamics of prestressed elastic lattices: Homogenization, instabilities, and strain localization. *J. Mech. Phys. Solids* **146**, 104198.

[26] Chen BG, Liu B, Evans AA, Paulose J, Cohen I, Vitelli V, Santangelo CD. 2016. Topological mechanics of origami and kirigami. *Phys. Rev. Lett.* **116**, 135501.

[27] Zheng L-Y, Teocharis G, Tournat V, Gusev V. 2018. Quasitopological rotational waves in mechanical granular graphene. *Phys. Rev. B* **97**, 060101(R).

[28] Li S, Kim I, Iwamoto S, Zang J, Yang J. 2019. Valley anisotropy in elastic metamaterials. *Phys. Rev. B* **100**, 195102.

[29] Prodan E, Prodan C. 2009. Topological phonon modes and their role in dynamic instability of microtubules. *Phys. Rev. Lett.* **103**, 248101.

[30] Wang P, Lu L, Bertoldi K. 2015. Topological phononic crystals with one-way elastic edge waves. *Phys. Rev. Lett.* **115**, 104302.

[31] Nash LM, Kleckner D, Read A, Vitelli V, Turner AM, Irvine WTM. 2015. Topological mechanics of gyroscopic metamaterials. *Proc. Natl. Acad. Sci.* **112**(47), 14495–14500.

[32] Garau M, Carta G, Nieves MJ, Jones IS, Movchan NV, Movchan AB. 2018. Interfacial waveforms in chiral lattices with gyroscopic spinners. *Proc. Roy. Soc. A* **474**, 20180132.

[33] Lee CH, Li G, Jin G, Liu Y, Zhang X. 2018. Topological dynamics of gyroscopic and Floquet lattices from NewtonâĂŹs laws. *Phys. Rev. B* **97**, 085110.

[34] Mitchell NP, Nash LM, Irvine WTM. 2018. Tunable band topology in gyroscopic lattices. *Phys. Rev. B* **98**, 174301.

[35] Garau M, Nieves MJ, Carta G, Brun M. 2019. Transient response of a gyro-elastic structured medium: Unidirectional waveforms and cloaking. *Int. J. Eng. Sci.* **143**, 115–141.

[36] Nieves MJ, Carta G, Pagneux V, Brun M. 2020. Rayleigh waves in micro-structured elastic systems: Non-reciprocity and energy symmetry breaking. *Int. J. Eng. Sci.* **156**, 103365.

[37] Nieves MJ, Carta G, Pagneux V, Brun M. 2021. Directional control of Rayleigh wave propagation in an elastic lattice by gyroscopic effects. *Front. Mater.* **7**, 602960.

[38] Carta G, Colquitt DJ, Movchan AB, Movchan NV, Jones IS. 2019. One-way interfacial waves in a flexural plate with chiral double resonators. *Philos. Trans. R. Soc. A* **378**(2162), 20190350.

[39] Carta G, Colquitt DJ, Movchan AB, Movchan NV, Jones IS. 2020. Chiral flexural waves in structured plates: directional localisation and control. *J. Mech. Phys. Solids* **137**, 103866.

[40] Wu L-H, Hu X. 2015. Scheme for achieving a topological photonic crystal by using dielectric material. *Phys. Rev. Lett.* **114**, 223901.

[41] Smith MJA, McPhedran RC, Meylan MH. 2013. Double Dirac cones at $\kappa = 0$ in pinned platonic crystals. *Waves Random Complex Media* **24**(1), 35–54.

[42] McPhedran RC, Movchan AB, Movchan NV, Brun M, Smith MJA. 2015. 'Parabolic' trapped modes and steered Dirac cones in platonic crystals. *Proc. R. Soc. Lond. A* **471**, 20140746.

[43] Evans DV, Porter R. 2007. Penetration of flexural waves through a periodically constrained thin elastic plate in *vacuo* and floating on water. *J. Eng. Math.* **58**, 317–337.

[44] Haslinger SG, Movchan NV, Movchan AB, McPhedran RC. 2012. Transmission, trapping and filtering of waves in periodically constrained elastic plates. *Proc. R. Soc. Lond. A* **468**, 76–93.

[45] Poulton CG, Movchan AB, Movchan NV, McPhedran RC. 2012. Analytic theory of defects in periodically structured elastic plates. *Proc. R. Soc. Lond. A* **468**, 1196–1216.

[46] Haslinger SG, Movchan NV, Movchan AB, Jones IS, Craster RV. 2017. Controlling flexural waves in semi-infinite platonic crystals with resonator-type scatterers. *Q. J. Mech. Appl.* **70**:(3), 216-247.

[47] Haslinger SG, Jones IS, Movchan NV, Movchan AB. 2018. Localisation in semi-infinite herringbone waveguides. *Proc. R. Soc. Lond. A* **474**, 20170590.

[48] Morvaridi M, Carta G, Brun M. 2018. Platonic crystal with low-frequency locally-resonant spiral structures: wave trapping, transmission amplification, shielding and edge waves. *J. Mech. Phys. Solids* **121**, 496–516.

[49] O'Neill J, Selsil Ö, McPhedran RC, Movchan AB, Movchan NV. 2015. Active cloaking of inclusions for flexural waves in thin elastic plates. *Q. J. Mech. Appl. Math.* **68**, 263–288.

[50] Miniaci M, Marzani A, Testoni N, De Marchi L. 2015. Complete band gaps in a polyvinyl chloride (PVC) phononic plate with cross-like holes: numerical design and experimental verification. *Ultrasonics* **56**, 251–259.

[51] Kherraz N, Radzieński M, Mazzotti M, Kudela P, Bosia F, Gliozzi AS, Misseroni D, Pugno NM, Ostachowicz W, Miniaci M. 2021. Experimental full wavefield reconstruction and band diagram analysis in a single-phase phononic plate with internal resonators. *J. Sound Vib.* **503**, 116098.

[52] Miranda Jr EJP, Nobrega ED, Ferreira AHR, Dos Santos JMC. 2019. Flexural wave band gaps in a multi-resonator elastic metamaterial plate using Kirchhoff-Love theory. *Mech. Syst. Signal Process.* **116**, 480–504.

[53] Miranda Jr EJP, Nobrega ED, Rodrigues SF, Aranas Jr C, Dos Santos JMC. 2020. Wave attenuation in elastic metamaterial thick plates: Analytical, numerical and experimental investigations. *Int. J. Solids Struct.* **204–205**, 138–152.

[54] Movchan AB, McPhedran RC, Carta G, Craster RV. 2019. Platonic localisation: one ring to bind them. *Arch. Appl. Mech.* **89**, 521–533.

[55] Movchan AB, McPhedran RC, Carta G. 2021. Scattering reduction and resonant trapping of flexural waves: two rings to rule them. *Appl. Sci.* **11**(10), 4462.

[56] Maz'ya VG, Movchan AB, Nieves MJ. 2013. *Green's Kernels and Meso-scale Approximations in Perforated Domains*. Lecture Notes in Mathematics 2077, Springer.

[57] Maz'ya VG, Movchan AB, Nieves MJ. 2020. On meso-scale approximations for vibrations of membranes with lower-dimensional clusters of inertial inclusions. *Algebra i Analiz* **32**(3), 219–237.

[58] Antonakakis T, Craster RV, Guenneau S. 2013. High-frequency homogenization of zero-frequency stop band photonic and phononic crystals. *New J. Phys.* **15**, 103014.